Oil palm empty fruit bunch valorization for activated and non-activated carbon nanoparticles and its heavy-metal-removal efficiency

Salma Zubaidah, Adisti Permatasari Putri Hartoyo, Januard Kristian Sihombing, Elis Nina Herliyana, Saptadi Darmawan, Nela Rahmati Sari, Muhammad Naufal Ibrahim Prabowo, Imam Hermawan, Isna Maulida and Achmad Solikhin

ABSTRACT

In this study, we examined activated and non-activated carbon nanoparticles (CNPs) derived from oil palm empty fruit bunch (OPEFB) fibers for their nanomaterial characteristics and their potential effectiveness in heavy metal removal. To investigate these properties, transmission electron microscopy, scanning electron microscopy (SEM), EDX, Fourier transform infrared spectroscopy, particle size analysis, X-ray diffraction, and atomic absorption spectrophotometry were employed. This study shows that both the activated and the non-activated CNPs were in the form of well-dispersed and aggregated particles. As analyzed using SEM, the external surfaces of the non-activated CNPs were determined to be irregular, while those of the activated CNPs had a more circular shape without aggregation. Carbon was the most dominant element observed in these CNPs, and the occurrence of its activation process altered the chemical functional groups of the non-activated CNPs by shifting their wavenumbers and intensities. Additionally, the activation process increased the crystallinity domain in the activated CNPs. OPEFB fibers could be valorized to obtain both activated and non-activated CNPs that had the potential efficiency to remove heavy metals, including copper (Cu), lead (Pb), iron (Fe), and zinc (Zn) at certain times. Based on the analysis of the Langmuir and Freundlich models, the activated and non-activated CNPs were found to have shown favorable adsorption to Cu, Pb, and Fe, with a percentage of heavy metal removal of over 84%. The adsorption of heavy metals was carried out via a chemical process.

Key words | carbon nanoparticles, heavy metals removal, nanomaterial characterizations, oil palm valorization

HIGHLIGHTS

- Nanocarbon based oil palm lignocellulose.
- Isolation method for nanocarbon.
- Comparative characteristics of nanocarbon.

Salma Zubaidah
Adisti Permatasari Putri Hartoyo
Januard Kristian Sihombing
Elis Nina Herliyana
Imam Hermawan
Isna Maulida
Silviculture Department, Faculty of Forestry and Environment,
Bogor Agricultural University (IPB University),
Bogor, West Java,
Indonesia

Saptadi Darmawan
Nela Rahmati Sari
Forest Products Research and Development Center,
Ministry of Environment and Forestry,
Bogor, West Java,
Indonesia

Muhammad Naufal Ibrahim Prabowo
Aquatic Resources Management, Faculty of Fisheries and Marine Science,
Bogor Agricultural University (IPB University),
Bogor, West Java,
Indonesia

Achmad Solikhin (corresponding author)
Southeast Asia Regional Center for Tropical Biology (SEAMEO BIOTROP),
Southeast Asia Minister of Education Organization,
Bogor, West Java,
Indonesia
and
Indonesian Green Action Forum (IGAF),
Jepara, Central Java,
Indonesia
E-mail: *achmad_solikhin@apps.ipb.ac.id*

doi: 10.2166/wst.2021.166

GRAPHICAL ABSTRACT

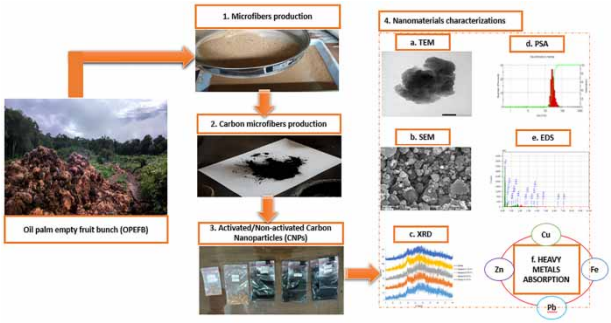

INTRODUCTION

With crude palm oil (CPO) production of 44.00 million metric tons in 2020, Indonesia has been referred to as the largest CPO producer in the world, followed by Malaysia and Thailand. Approximately 23% of OPEFB from oil palm total waste was generated from the production of CPO (Ichriani *et al.* 2016). Thus, the abundance of waste could be harnessed to obtain value-added products, such as water purifiers, geotextiles, composts, bio-composites, bio-ethanol, bio-pellets, bio-oil, and electricity.

The presence of disruptive technology, nanotechnology, has motivated researchers and industries to utilize OPEFB fibers as nanomaterial sources, such as nanocrystalline cellulose, nanofibrillated cellulose, and carbon nanotubes (Deraman *et al.* 2010; Goh *et al.* 2016; Al-Dulaimi & Wanrosli 2017). In addition to these nanomaterials, carbon nanoparticles (CNPs), which are also well-known carbon nanofibers (CNFs), are another bionanomaterial that can be derived from OPEFB. However, there have not yet been any reported studies concerning the isolation of CNPs from OPEFB, although some research reported on the isolation of carbon fibers by pyrolysis or the carbonization-activation process derived from OPEFB for a variety of uses (Farma *et al.* 2013; Osman *et al.* 2016).

CNPs isolated from biomass can be obtained by several means, such as electrospinning, pyrolysis, hydrothermal treatment, ultrasonication, and chemical vapor deposition (Chen *et al.* 2009; Azwar *et al.* 2018). CNPs are expected to revolutionize several fields in material science and nanotechnology due to their incredible properties, such as their electron, biomimetic form, high electrical conductivity, and unique surface properties (Smolka *et al.* 2019). With the treatment of the physical and/or chemical activation processes, superior adsorption capacity is the aim of producing activated CNPs. With the treatment, activated CNPs are expected to be used as a liquid or a gas purifier.

Previous studies have been undertaken to examine the purpose of CNPs as a pollutant purifier. For instance, Jahangiri *et al.* (2013) have studied the activated carbon (AC) and CNF composites used for the adsorption of volatile organic compounds and for respirator cartridges. Maddah *et al.* (2016) also examined activated CNFs as an efficient sorbent for determination and preconcentration of organophosphorus pesticides in water samples. However, CNPs have also been studied for water purification, especially nanoparticles, organic solvents, methylene blue, and cationic and anionic heavy metals (Park *et al.* 2000; Liang *et al.* 2011; Faccini *et al.* 2015; Santhosh *et al.* 2017). In this study, OPEFB fibers were harnessed as raw materials for both activated and non-activated CNPs; these CNPs were also investigated with regard to their nanomaterial properties, including their potentials as water purifiers.

METHOD

Materials

OPEFB fibers were obtained from IPB University Cikabayan Palm Oil Plantation and PT Perkebunan Nusantara (PTPN) VIII, Bogor, West Java, Indonesia. The chemicals used for the production of the nanocarbon particles were hydrogen chloride (HCl) and potassium hydroxide (KOH) (Merck KGaA, Darmstadt, Germany), as well as copper (Cu), lead (Pb), iron (Fe), and zinc (Zn) heavy metals at different concentrations (Chemistry Department, IPB University, Indonesia).

OPEFB microfiber production

The OPEFB fibers were submerged and washed with detergent and water in order to remove sand, stones, mud, soil, and wax. After washing, clean OPEFB fibers were obtained and air-dried before being processed with milling. Then, a dry-disk milling machine, with an AC motor (Siemens TEC 112M, Germany), was used to pulverize the OPEFB fibers with a 100-mesh to 200-mesh size range (0.149–0.074 mm). The fibers were fed into the machine for approximately 10–20 min to obtain the intended particle size. The particles were then air dried for approximately 5 days until a 15–20% moisture content sample was obtained. Afterward, the sample was referred to as OPEFB microfibers.

Carbon microparticle production

Prior to pyrolysis process, the OPEFB microfibers (<0.074 mm) were pulverized using a conventional blender to obtain finer fibers. Approximately 1 kg of OPEFB microfibers was pyrolyzed and carbonized using a modified carbonization reactor (Research, Development, and Innovation Agency; Ministry of Environment and Forestry; Bogor, Indonesia) for 3 h with a temperature of 400 °C and pressure of 2 bar, as well as a limited oxygen presence. The yield of the carbonization was 88% or 880 g of OPEFB carbon microfibers. Approximately 2 g of OPEFB carbon microfibers were further processed using a vibrational pressurized mill (Herzog HSM 100P Maschinenfabrik GMBH Co., Germany) to obtain micro-sized particles of carbon. The milling was carried out with a voltage of 380 V, a frequency of 50 Hz, and power consumption of 1.9 kVA, as well as a pressure range between 5 and 6 bar. These microfibers were then ground for 3 min, and the grinding was repeated 10 times, which means that the actual milling time was approximately 30 min, excluding the paused time.

Activated and non-activated carbon nanoparticle isolation

After the Herzog milling process, the milled particles were then processed to produce activated or non-activated micro-sized nanoparticles. For the activated micro-sized nanoparticles, the Darmawan (2014) modified activation method was used, including the KOH precursor-assisted hydrothermal process and HCl treatment. The hydrothermal process was undertaken for 30 min at a temperature of 800 °C, whereas the activation process was run at a ratio between the KOH and the OPEFB carbon microparticles of 1:3 (w/w). Before the hydrothermal process, approximately 150 g of the particles was soaked for 24 h in a 1.37 M KOH solution in which the initial weight of the KOH powder used for the solution was 50 g. Next, the particles were dried at 60 °C for 24 h and were activated to reach 800 °C. When this temperature was reached, water vapor was directed into the reactor for 30 min. The activation process was then subsequently continued with the washing of the activated OPEFB carbon microparticles with 10% HCl, followed by hot water, to remove impurities and neutralize the pH. The activated OPEFB microparticles obtained were subsequently air-dried to remove the remaining water. By comparison, the non-activated OPEFB microparticles were prepared, but the microparticles were produced with the activation method. The non-activated microparticles were isolated immediately after the Hertzog milling process.

To obtain the CNPs, approximately 1 g of activated or non-activated carbon microparticles was submerged into 100 ml of distillate water. Ultrasonication was conducted using an ultrasonic machine (Ultrasonic Processor, Cole-Parmer, USA) fitted with a 6-mm (1/400) titanium probe and tip, and a footswitch connector, for 45 min with the following parameters: 45% of amplitude, 130 W of power, and 20 kHz of frequency. Both the activated and the non-activated CNPs were subsequently centrifuged for 10 min to separate the precipitated CNPs (pellet) and the supernatant. The pellet was then tested using several instruments, such as transmission electron microscopy (TEM), scanning electron microscopy (SEM), Fourier transform infrared (FT-IR) spectroscopy, X-ray diffraction (XRD), and particle size analysis (PSA); its heavy-metal-removal efficiency was also investigated.

Characterizations

Both the activated and the non-activated CNPs, which were air-dried, were tested with regard to their morphology and external surfaces using an analytical SEM (SEM JSM-6510A, Japan). Before this analysis, gold was used for coating the surfaces and the morphology of the CNPs (JEOL JFC 1600, Japan) at an acceleration voltage of 10 kV. Analysis with a TEM (TEM FEI Tecnai G2 20 S-Twin, USA) was used to investigate the nano-sized structure of the CNPs. Prior to testing, the CNP solution (0.05 mg/mL) was dropped into a TEM micro-grid and stained with a 1% uranyl acetate solution. The stained micro-grid was subsequently blotted off and air-dried.

The nanoparticle size distribution (Z-average, PDI, and size distribution by number) of these CNFs was measured with a PSA (PSA Malvern Panalytical, Zetasizer Ver. 7.13

Serial Number: MAL1059778). The measurement was carried out at a temperature of 25.1 °C, with a count rate of 111.9 kcps, a duration of 50 sec, and a measurement position of 3.00 mm. The chemical functional group changes of the CNPs were analyzed with FT-IR (FT-IR OPUS Bruker, Canada) within a wave number range of 500–4,000 cm^{-1} and with a resolution of 2 cm^{-1}.

The dried CNP powders were also analyzed using an XRD (XRD 6100 Shimadzu, Japan) with Cu Kα irradiation (1.54 Å, 40 kV, and 30 mA) within a 2θ degree of 10°–80°, a sampling pitch of 2θ = 0.02°, and a scan speed of 2.00°/min. To investigate the effectiveness of these CNPs in absorbing heavy metals (Fe, Zn, Pb, and Cu), an AAS was used. The different initial concentrations of the heavy-metal solutions (8.76 ppm (Fe), 4.18 ppm (Zn), 11.18 ppm (Pb), and 12.56 ppm (Cu)) were purchased from the Chemistry Department, IPB University. These solutions were prepared by micro-pipetting a certain amount of heavy metal into a 10 mL measuring flask and diluting it to achieve 10 ml with distilled water. By comparison, controlled samples were prepared. Approximately 0.1 mg of these CNPs was mixed with 10 ml of distilled water (control) and was then mixed with 10 ml of heavy-metal solution. Varied times for testing (0, 30, and 60 min) were utilized. The testing of heavy-metal adsorption was carried out at room temperature in the Chemistry Laboratory of IPB University (approximately 20 °C ±3 °C).

The adsorption isotherms were investigated using the Langmuir and Freundlich models. These models were used to calculate certain parameters under Langmuir and Freundlich expressions and to describe the heavy-metal adsorption onto the nanomaterials including homogenous or heterogeneous solids. The formulas of the Langmuir model (1) and the Freundlich model (2) can be expressed linearly as follows.

(1) Langmuir model

$$\frac{Ce}{qe} = \frac{1}{qm\ Kl} + \frac{Ce}{qm}$$

The nature of the Langmuir process can be analyzed using Rl, and the formula of Rl can be expressed below:

$$Rl = \frac{1}{1 + Kl\ Co}$$

Rl > 1 is unfavorable, Rl is linear, 0 < Rl < 1 is favorable, and Rl = 0 is irreversible, where Ce = the equilibrium concentration of the adsorbates (mg L^{-1}), qe = the equilibrium adsorption uptake of the adsorbates (mg g^{-1}), qm = the maximum monolayer capacity (mg g^{-1}), Kl = the Langmuir constant (L mg^{-1}), Rl = the separation factor, and Co = the initial concentration of the adsorbates (mg L^{-1}).

(2) Freundlich model

$$log\ qe = N\ log\ Ce + log\ Kf$$

where qe = the equilibrium adsorption uptake of the adsorbates (mg g^{-1}), Kf = the Freundlich adsorption constant ((mg g^{-1}) (L $mg^{-1})^{1/n}$), Ce = the equilibrium concentration of the adsorbates (mg L^{-1}), N = the empirical constant, and n_f = the adsorption intensity.

RESULTS AND DISCUSSION

Nano-sized structures

Figure 1 shows the activated and non-activated CNP solutions. Most of the CNPs were observed to possess the feature of being particles with good dispersion and aggregation appearance. The activated CNPs were observed to be distributed well in the suspension with a size of below 100 nm, although some aggregates were also found (shown by the red arrow in Figure 1(a) and 1(b)). Additionally, the non-activated CNPs were mostly aggregated into large particles (shown by the red arrow in Figure 1(c) and 1(d)) with a size of over 100 nm. In this study, the activated CNPs tended to not be much aggregated, presumably due to the active presence of electrostatic/steric repulsive forces between the individual CNPs. The forces were generated from the chemical activation processes of the CNPs using the chemical–hydrophysical treatment. It was also noted that the aggregations of non-activated CNPs were due to van der Waals forces (Atif & Inam 2016). The aggregates also brought about the presence of electrostatic attractions (Koh & Cheng 2014). The retardation of the aggregations in the activated CNPs was presumably due to the activation processes (KOH treatment, hydrothermal process, and HCl treatment). Three important reasons for the hampering of individual CNP aggregates in water can be described as follows:

1. KOH-activated carbon nanoparticles can decrease oxygen-, nitrogen-, and hydrogen-based active sites, especially oxygen-containing functional groups, such as hydroxyl groups that have a high tendency to form

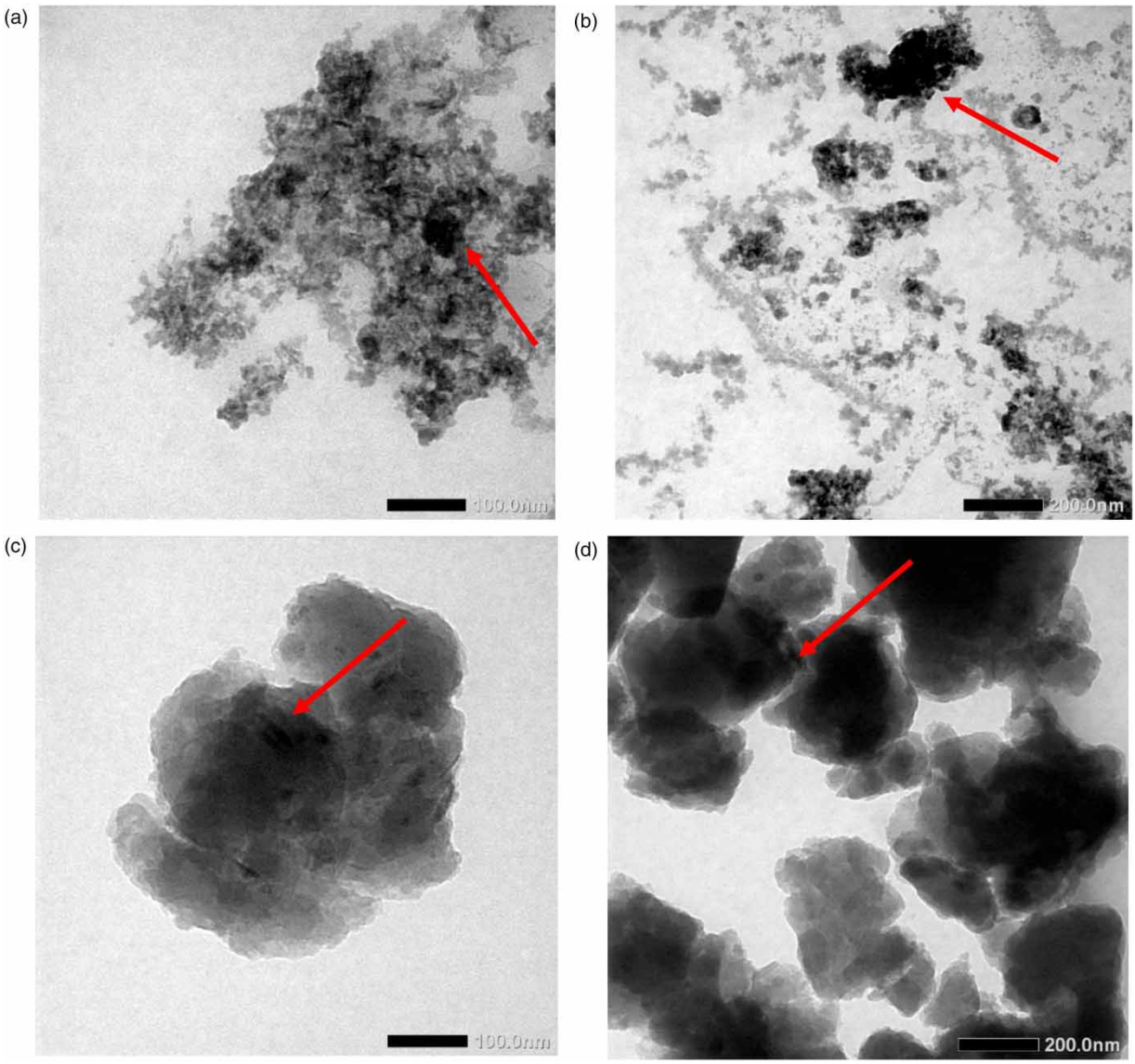

Figure 1 | Nano-sized carbon of activated OPEFB CNPs (a) and (b) and non-activated OPEFB CNPs (c) and (d).

hydrogen bondings with water and to create aggregations of CNPs. According to Romanos *et al.* (2011), the KOH treatment could also decrease oxygen, nitrogen, and hydrogen content, but increase carbon content. Additionally, KOH was utilized to create tunable sub-nanometer and supra-nanometer pores, leading to the increase in surface area and porosity of the CNPs. This was also in line with the study conducted by Perez-Salcedo *et al.* (2020), which stated that KOH activation improved the biocarbon performance since the physical–chemical properties were enhanced, including the surface area, the microporosity, the pore volume, and the defective sites.

2. KOH activation combined with the hydrothermal process could increase and control the specific surface area, the ordering degree, the hierarchical pore, the graphene-like sheets, and the carbon content while lowering the oxygen, hydrogen, and nitrogen elements. With the increase of the ordering degree, the crystalline region mostly dominated the CNPs, leading to the decrease in a free and reactive amorphous domain, which, in turn, generates aggregates. Additionally, the decrease in oxygen, hydrogen, and nitrogen contents that comprised the oxygen-containing functional groups in the CNPs could have hampered the aggregation of

the CNPs. These phenomena were in line with the studies by Pari *et al.* (2014), Liu *et al.* (2020), and Ye *et al.* (2020).

3. HCl treatment could remove an amorphous region of the carbon that was very free and reactive, causing aggregations of the individual CNPs. From the study conducted by Fan *et al.* (2010), HCl treatment could remove the amorphous region and peel off the external layers with defects in the multi-walled carbon nanotubes (MWCNTs).

Furthermore, to reduce the aggregates, it is recommended to harness the surfactant using mechanical treatments (homogenization, ultrasonication, ball milling, grinding, and cryomilling) and surface modifications (coating, functionalization, and stabilization). For instance, Li & Qiu (2019) reported that the use of surfactants, such as TX100 and sodium dodecyl sulfate (SDS), could create stable dispersion on the MWCNTs by lowering the surface tension of the CNPs. These surfactants then became adsorbed by way of their hydrophobic group onto the MWCNTs' exterior surface via non-covalent attraction forces, leading to improved dispersion. The properties of the obtained nanocomposites, especially the mechanical properties and the interfacial/interphase properties, would have been affected if the aggregated CNPs were not broken down into individual CNPs. In terms of heavy-metal adsorption, the aggregations could generate decreased adsorbing properties and alter the properties of the bare CNPs through the decrease in their surface area, their surface area-to-volume ratio, and their affinity.

Morphology and external surface

Figure 2 shows the oven-dried samples of non-activated and activated CNPs. Both of these types of CNPs had irreversible aggregated nanofibers with an uneven circular shape. However, as compared with the non-activated CNPs, the activated CNPs had a few aggregations, almost forming an individual steady circular-shape state. This condition was similar to the previous study conducted by Pari *et al.* (2014) in which porous carbons activated using hydrothermal carbonization and KOH were noted to have spherical shapes with several agglomerated carbon clusters. That was because of the consecutive activation processes, combining KOH treatment, hydrothermal activation, and HCl treatment. These treatments could have increased the surface area and controlled the formation of the hierarchical pores, removing the amorphous domains, leading to the formation of graphene-like sheets with high crystallinity. Additionally, these treatments could have reduced the oxygen, nitrogen, and hydrogen contents in which the oxygen-containing functional groups that were decreased could have reduced the aggregations of the individual CNPs. Through the process, the activated CNPs would presumably have had a balanced hydrophobic–hydrophilic side, generating a stable material in an aqueous solution. The aggregation size of the activated CNPs was more than 1 μm, and there were still individual activated CNPs with sizes below 1 μm. This was very distinct with the non-activated CNPs, with interconnected-like aggregations with a size of over 1 μm. The aggregation of these nanofibers was due to the hornification process during oven-drying. The aggregations were mostly in the form of homoaggregates rather than the formation of heteroaggregates (aggregations of each individual CNP with uniform diameter). In addition, the phenomenon was due to the presence of electrostatic attractions instead of van der Waals or hydrophobic interactions resulting from the correlations between the screening counterions (Koh & Cheng 2014). This was pursuant to the study of Niyogi *et al.* (2007), which demonstrated that single-walled carbon nanotubes have electrostatic repulsion between the nanotubes leading to aggregation. In the solid state (dried CNPs), the aggregation was deemed irreversible, whereas in suspension the aggregation was reversible. To prevent the aggregation in the liquid/suspension state, the surfactant, for example, SDS, was utilized (Niyogi *et al.* 2007, Tummala & Striolo 2009). Shear-mixing and sonication could also have been used to create good dispersion of the carbon nanotubes and to break down the large agglomerates. These mechanical means had the sufficient energy density needed to overcome the internal forces holding the aggregates together (Keinänen *et al.* 2018). However, Arora & Attri (2020) reported that the aggregations could have caused beneficial and detrimental effects on the adsorption of the heavy metals, depending on the types of carbon nanotubes. The detrimental effect would have been due to the reduction of the total surface areas of the CNPs, which could lead to the decrease in bulk pollutants adsorbed. However, the beneficial effect would have been the creation of interstitial channels and grooves in the peripheral spaces of the CNP bundles, leading to the creation of trapping for contaminants.

Particle size analysis

Table 1 shows the particle size analysis of the non-activated and activated CNPs. Both the non-activated and the activated CNPs have been determined to have high Z-average and average size distributions by number, volume, and

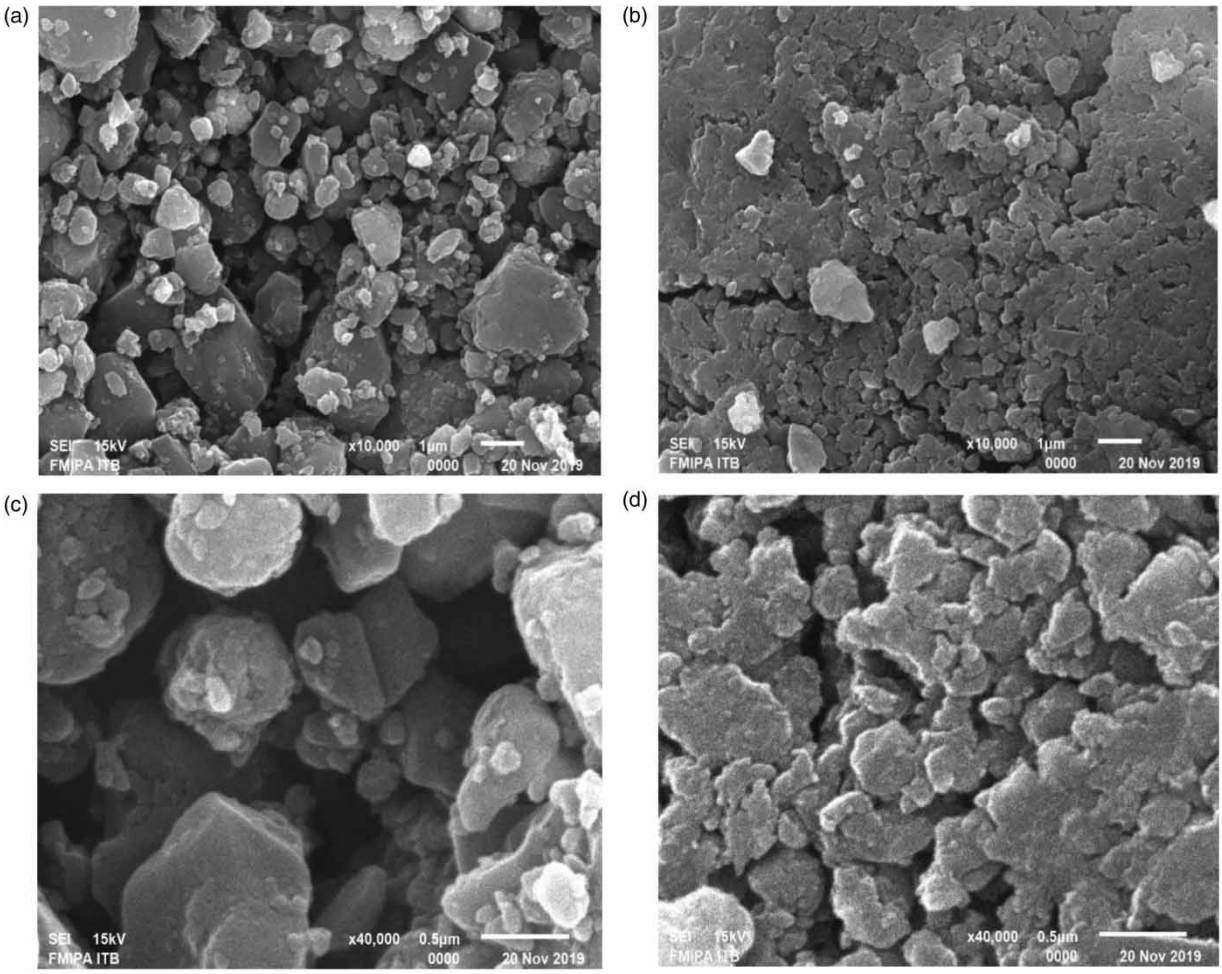

Figure 2 | Morphology of activated OPEFB CNPs (a) and (b) and non-activated OPEFB CNPs (c) and (d).

Table 1 | Particle size analysis by number, volume, and intensity

		Intensity (nm)		Volume (nm)		Number (nm)	
Sample	**Peak**	**Mean**	**Width**	**Mean**	**Width**	**Mean**	**Width**
Non-activated CNPs	I	749.13	89.52	774.87	122.76	742.27	118.20
	II	844.01	166.63	917.95	199.67	817.12	185.76
	III	949.16	235.95	1078.31	271.32	900.19	249.72
Average		847.43	164.03	923.71	197.92	819.86	184.56
Activated CNPs	I	368.10	98.47	344.93	108.04	281.87	74.72
	II	360.25	143.35	340.75	154.98	110.78	19.78
	III	430.70	133.27	423.46	160.71	306.70	99.55
Average		386.35	125.03	369.71	141.24	233.11	64.68

intensity above 100 nm. The non-activated CNPs had a higher Z-average and size distribution by number, volume, and intensity than those of the activated CNPs.

For instance, in Table 1 and Figure 3 (Peak I), the Z-average (746.0 nm) and the particle size distribution by number (742.3 nm) of the non-activated CNPs were higher

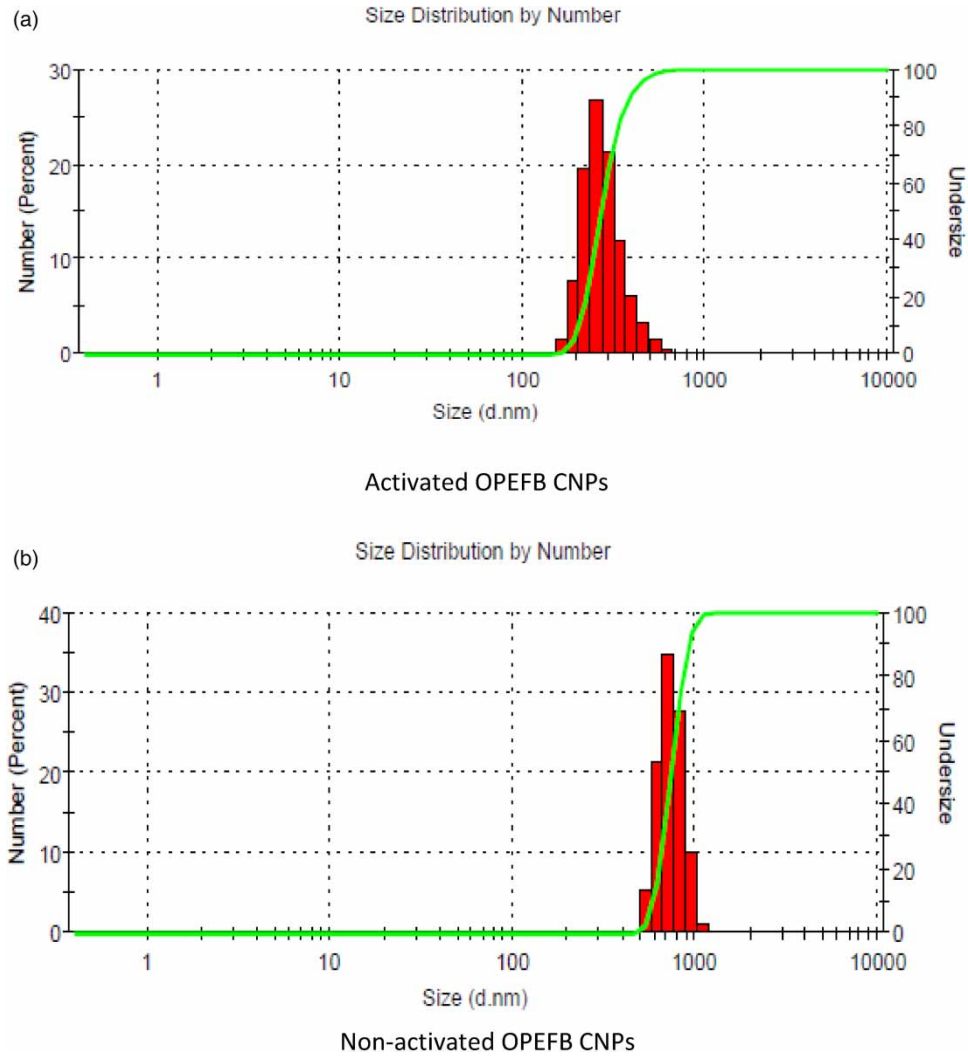

Figure 3 | Particle size distribution of activated (a) and non-activated OPEFB CNPs (b) for peak I.

than the Z-average (321.3 nm) and the particle size distribution by number (281.9 nm) of the activated CNPs. Additionally, the PDIs of the non-activated and the activated CNPs were 0.106 and 0.073, respectively, which shows that activated CNPs had moderate polydisperse (0.1–0.4), whereas the non-activated CNFs had uniform polydisperse, indicating that the non-activated CNFs had good homogeneity in an aqueous solution. The moderate polydisperse of the activated CNPs could be noted due to the presence of homogenous aggregates bundled together with uniform nanoparticles. This could also be seen from the distribution mode, and the distribution mode of the activated and the non-activated CNPs was unimodal (one peak), without any appearance of bimodality (two peaks) and multimodality (multiple peaks over two peaks). The absence of bimodality and/or multimodality was presumably because of (1) mixed multiple particles, (2) aggregate size groups under the agglomerated CNPs, and (3) the breakdown of large particles. However, the presence of aggregates could not be fully considered to give negative effects because the aggregates could have formed interstitial channels and grooves for trapping heavy metals. From this study, the PSA analysis could not be compared with the TEM analysis as the PSA measured the equivalent hydrodynamic diameter and the intensity-weighted distribution, whereas the TEM provided the number-weighted distribution. However, it could be seen that there were aggregates of both non-activated and activated CNPs in an aqueous solution, which were generated by electrostatic attractions and/or hydrophobic interactions. According to Li & Qiu (2019), the formation of aggregates, thick bundles, and ropes in carbon nanotubes is brought about by strong van der Waals interactions along

the length axis. If this condition were maintained during the drying process, the hornification of these CNFs would lead to an irreversible aggregation (Figure 1).

Elemental analysis

Figure 4 shows the elemental analysis of the activated and non-activated CNFs. Both the activated and non-activated CNFs consisted of C, O, Na, Mg, Al, Si, Cl, K, Ca, and Fe with different percentages of mass. The two dominant elements were carbon and oxygen, indicating that these CNFs were a lignocellulose source. The non-activated CNFs had a smaller percentage of oxygen than the activated CNFs. This was due to the existence of an amorphous region of the activated CNPs, which had remained. At the preliminary stage, the activation of the CNFs used the chemical method; oxygen was present at higher levels than in the non-activated carbon, and it started to decrease due to the removal of the oxygen-containing functional groups in the carbon skeleton during the physical activation carbon method (high temperature at 800 °C). The presence of oxygen-containing groups (–OH and –COOH) was highly expected because the groups played an important role in the adsorption of heavy metals. Furthermore, the previous studies of Yang *et al.* (2019) and Bian *et al.* (2015) reported that adding heteroatoms, primarily oxygen, nitrogen, and sulfur, through surface modifications onto the carbon surfaces, enhanced the surface functionalities and the sorptive properties to heavy metals in the aqueous solutions. This was because of the improvement of the surface properties of the carbon adsorbents, including the specific surface area, the pore size distribution or the pore volume, the increment of the functional groups' presence, and the enhancement of their structural stability. However, the percentage of oxygen in the activated CNFs was still higher than that in the non-activated CNFs. Other predominant elements were Al, Si, Cl, K, Ca, and Fe, indicating the remaining impurities in these CNFs. For instance, Si is associated with silica compounds deposited in OPEFB fibers.

Crystallographic pattern

The crystallographic pattern of the activated CNPs and the non-activated CNPs is presented in Figure 5. There is a difference in the peak patterns that appear for both the activated CNPs and the non-activated CNPs. The two highest peaks are for the activated CNPs; namely, the broad peak at 26° to 29° and a sharp peak at 35°, indicating the appearance of a crystalline domain or the growth of graphitic micro-crystallites. However, for the non-activated CNPs, there is only one highest peak at 23°. The highest peak of the non-activated CNPs, a basal reflection (002) peak at $2\theta = 23°$, indicates the formation of a graphitic structure (Arie *et al.* 2017). According to Aqel *et al.* (2012), carbon nanotubes are composed of a graphitic structure with an enrolled cylindrical sheet of graphene, which is rolled up into a seamless cylinder with a diameter of the order of a nanometer. After the activation process, the peak shifted to a broad peak ranging from 26° to 29°. This shift was due to the change of the atomic distance of the activated carbon that was caused by the interlayer spacing changes (Farma *et al.* 2017). Additionally, a new peak at 35° appeared, and its intensity was also noted to increase,

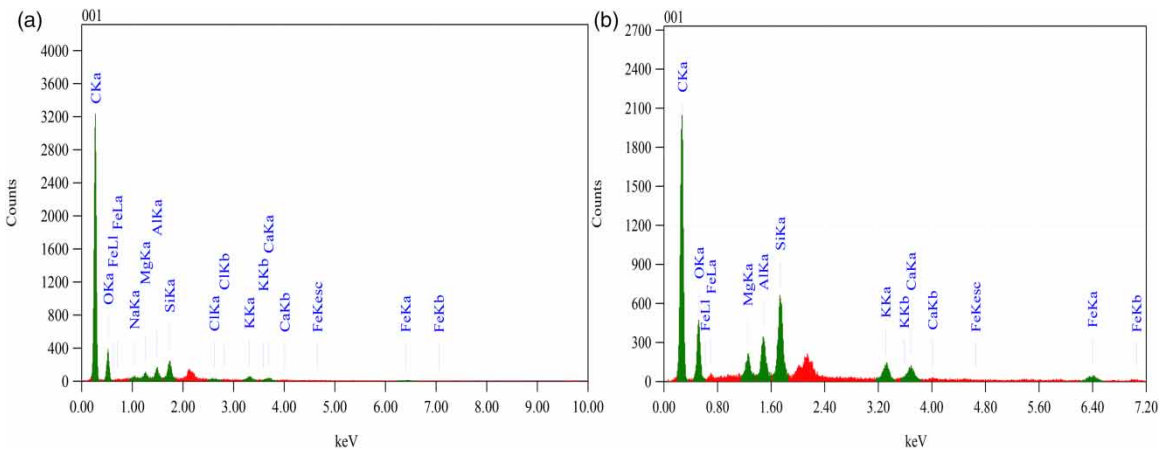

Figure 4 | Elementals analysis of activated and non-activated CNPs.

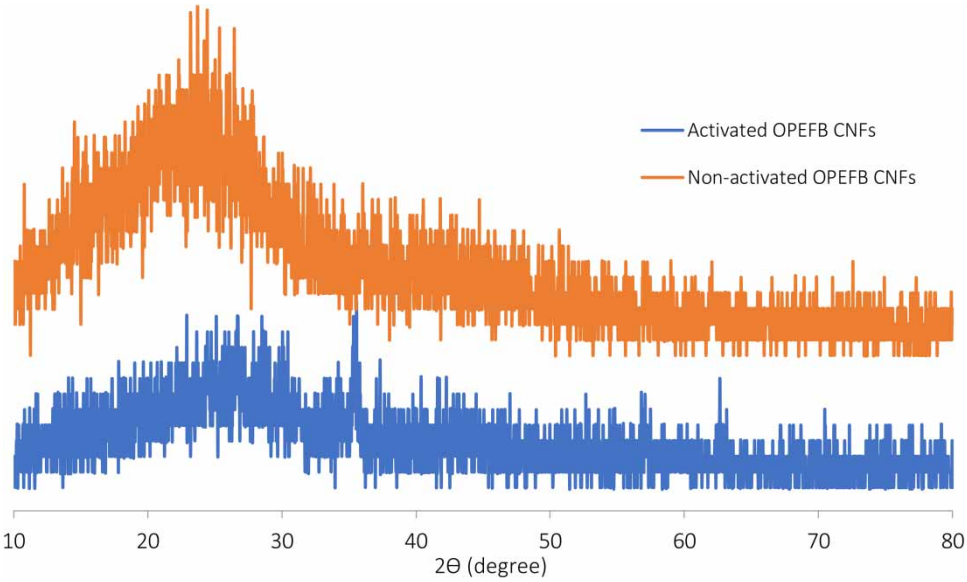

Figure 5 | XRD pattern of activated and non-activated OPEFB CNPs.

leading to the increase of crystallinity due to a more developed graphitic structure. This was pursuant with the increase in the crystallinity index of the activated CNPs (31.56%) over the crystallinity index (CrI) of the non-activated CNPs (31.11%). The remaining region in both the activated and the non-activated CNPs was the less-ordered region, which was well known to be an amorphous region. The region was more active than the crystalline region, leading to the facility of trapping heavy metals, and it could be easily found in carbon black and activated charcoal.

Chemical functional groups change

Figure 6 shows the chemical functional group changes of the activated and non-activated CNPs after analysis with FT-IR. Some indicative peaks of these CNPs are summarized in Table 2. There were shifted wavenumbers of non-activated CNPs to lower or higher wavenumbers after treatment with the activation process. The shifts were presumably due to chemical activation with KOH and HCl, and the physical activation at the high temperature of 800 °C. The

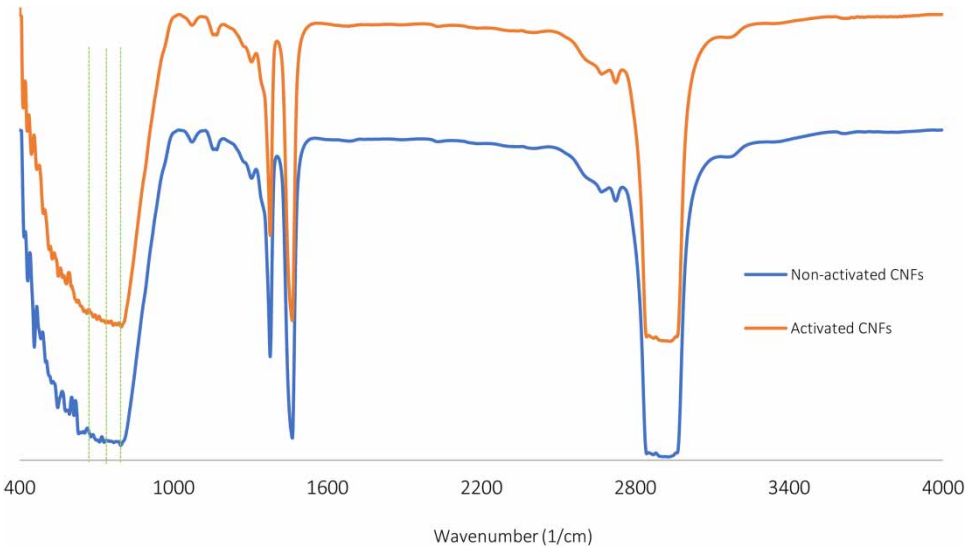

Figure 6 | Chemical functional group of activated and non-activated CNPs.

Table 2 | FTIR analysis of activated and non-activated CNPs

Wavenumber (1/cm)		
Activated CNPs	**Non-activated CNPs**	**Chemical functional groups**
699	700	C-H vibration (Ahmad *et al.* 2020)
765	729	NO_2 bending vibration (out of plane) in aromatic nitro groups (Mamun *et al.* 2016)
796	794	Ethyl groups (Jovanovic *et al.* 2009)
1376	1376	N-CH_3 (Misra *et al.* 2007)
1461	1461	CNT/MWCNTs vibrational modes (Misra *et al.* 2007)
2872	2871	C-H bonds (Azmina *et al.* 2011, Mamun *et al.* 2016)
2935	2929	C-H bonds (Azmina *et al.* 2011, Mamun *et al.* 2016)

peaks at 1,376 and 1,461 cm^{-1} were not changed, and these peaks indicated the vibrations of N-CH_3 and CNT/MWCNTs, respectively (Misra *et al.* 2007).

However, some of the identified peaks had shifted their wavenumbers, especially 2,871 and 2,929 cm^{-1}, and these peaks was designed with the presence of the C–H bond. In the wavenumber range of 400–1,000 cm^{-1}, the two peaks, namely, 729 and 794 cm^{-1}, which indicated NO_2 bending vibration and ethyl groups, respectively, were found to have shifted. Additionally, a peak of 699 cm^{-1} was also not found after the activation processes, indicating C–H vibration (Ahmad *et al.* 2020). There was also a change in the intensity of the wavelength along the 400–1,000 cm^{-1} band. The shift of these wavenumbers was presumably due to the activation treatment given to the CNPs. With the activation processes, the oxygen, nitrogen, and hydrogen contents were decreased, but the carbon content was increased, leading to the removal of the oxygen-containing functional groups. In addition, the removal of the amorphous domains, which mostly consisted of hydroxyl groups, was another reason for the shifted wavenumbers in the CNPs' FT-IR analysis.

Heavy-metal adsorption

Table 3 shows the adsorption of heavy metals (Cu, Pb, Fe, and Zn) by the activated and non-activated CNPs. These CNPs could effectively adsorb Cu, Pb, and Fe with an efficiency value of over 80%, whereas the adsorption of Zn was over 70%. The differences in the efficiency values were because the adsorbents (activated CNPs and non-activated CNPs) had selective removal of heavy metals due to their different affinities to the binding sites. This meant that these CNPs had the potential to be used as a bio-adsorbent for water contaminated with heavy metals. The effectiveness was presumably due to the excellent adsorption properties, adsorption sizes, and the large specific surfaces featuring strong van der Waals binding energy for the molecular adsorbates on well-defined adsorption sites, such as the interior tube sites, the groove sites, the exterior sites, and the interstitial sites (Mubarak *et al.* 2013). The activated CNPs had higher heavy-metal adsorption

Table 3 | Heavy metals absorption of activated and non-activated CNPs

Sample	Heavy metals	Time (min)	Initial concentration (ppm)	Final concentration (ppm)	Reduced concentration (ppm)	Effectiveness (%)
Cu	Activated CNPs	30	12.56	0.89	11.67	92.88
		60	12.56	1.92	10.65	84.74
	Non-activated CNPs	30	12.56	0.05	12.52	99.64
		60	12.56	0.06	12.50	99.49
Pb	Activated CNPs	30	11.18	0.22	10.97	98.07
		60	11.18	0.05	11.13	99.57
	Non-activated CNPs	30	11.18	0.21	10.97	98.08
		60	11.18	0.45	10.74	96.01
Fe	Activated CNPs	30	8.76	0.37	8.39	95.75
		60	8.76	0.11	8.65	98.70
	Non-activated CNPs	30	8.76	1.14	7.62	86.99
		60	8.76	1.02	7.74	88.33
Zn	Activated CNPs	30	4.18	1.47	2.71	64.82
		60	4.18	1.50	2.68	64.15
	Non-activated CNPs	30	4.18	1.27	2.91	69.62
		60	4.18	1.51	2.67	63.91

effectiveness for Pb and Fe than the non-activated CNPs. This was due to the effect of hydrochloric acid used for carbon-particle activation where chloride can react with these heavy metals, allowing for more effective removal of lead from the wastewater (Osman *et al.* 2019). Additionally, the KOH treatment was an activating agent for the CNPs, leading to an increase in the surface area and the pore volume. As compared with the previous studies, Mamun *et al.* (2018) have examined the potential of palm oil carbon nanotubes (CNFs) as an adsorbent for lead, with the sorption capacity of CNFs for lead ion removal in an aqueous solution of approximately 77 mg/L. Yusoff *et al.* (2019) also studied the removal of Cu(II), Pb(II), Cd(II), Zn(II), and Cr (IV) using oil palm decanter cake activated carbon in which the removal efficiencies of these metals were 45.01%, 64.26%, 7.14%, 39.21%, and 7.64%, respectively. Furthermore, Alam *et al.* (2008) also studied the utilization of activated carbon treated with 1,000 °C for 30 minutes, in which the activated carbon had a maximum Zn-adsorption capacity of approximately 98% in an aqueous solution. However, iron is mostly incorporated with CNPs as a functionalizing agent, for instance Fe_3O_4, to enhance not only the adsorption capacities but also the magnetic features (Li *et al.* 2015).

In this paper, the result of this heavy-metal adsorption study is contrasted with the results of other studies. In this study, the adsorbent dosage used was 0.1 g; with this dosage, a high number of adsorbates could be removed at a certain time. With regard to comparisons, there have been some previous studies on the use of oil palm biomass fibers and activated carbon for heavy metal removal. For instance, approximately 2,000 mg of oil palm kernel shell powders was used to remove Pb^{2+} and Zn^{2+} ions from water, with the highest percentage removal being 99.01% and 83.45%, respectively (Baby *et al.* 2019). A study by Elias *et al.* (2021) also reported that 10 g/L (10 g) of OPEFB activated carbon could remove 92.01% of Pb (II) after 15 min. Wahi *et al.* (2009) also examined the use of 200 and 1000 mg of OPEFB-activated carbon that could remove 100% of Pb and 25% of Cu, respectively. Furthermore, as compared with the efficiency of carbon nanoparticles for heavy metal removal, Bankole *et al.* (2019) studied the use of 20 mg of purified carbon nanotubes to remove Cu, Pb, Fe, and Zn, and their highest respective removal efficiencies of these metals were 93%, 99, 92, and 89%. It could be surmised that this study only harnessed the smallest amounts of CNPs, and the highest percentage of heavy metal removal was successfully attained. This phenomenon was due to the enhanced properties of both the activated and non-activated CNPs, including the surface area, the microporosity, the pore volume, and the defective sites. Although some CNPs were observed to aggregate, the aggregations could have provided the grooves, exteriors, and interstitial sites that had trapped many heavy-metal ions.

Adsorption isotherms

The adsorption isotherm models of heavy-metal removal by activated and non-activated CNPs can be seen in Table 4. In this study, the Langmuir and Freundlich equations were utilized to acquire the modeling adsorption data and to determine whether the measured parameters exhibited monolayer coverage prediction of the adsorbate or multilayer adsorption on the heterogeneous surface. From these models, certain parameters of the Langmuir and Freundlich isotherm equations were obtained, including the linear regressions, qm, Kl, Rl, Kf, *N*, nf, and R^2. Both the Langmuir and the Freundlich equations had a coefficient of determination (R^2) of 1 for the individual activated CNPs and the non-activated CNPs. This means that these equations provided an excellent fit due to their linearity, describing the potential of both the individual activated CNPs and the non-activated CNPs for the removal of Cu, Pb, Fe, and Zn. However, when the data of each nanomaterial were combined (activated CNPs/non-activated CNPs) for certain heavy metals, the Langmuir equation showed better linearity, in which the R^2 of the Langmuir form was higher than that of the Freundlich form. This shows that the removal of Cu, Pb, Fe, and Zn on the homogenous surface of the activated CNPs/non-activated CNPs occurred by way of monolayer adsorption or chemisorption.

The values of the heavy metal removal efficiencies were parallel with the value of qm in the Langmuir equation. The activated CNPs were noted to have a higher qm for Pb and Fe, whereas the non-activated CNPs had a higher qm for Cu and Zn. This indicated that these nanomaterials were favorable for removing certain heavy metals at the maximum monolayer adsorption capacity. For instance, the activated CNPs had the maximum Pb adsorption capacity of the monolayer adsorption at 1,000 (mg/g). Another parameter calculated under the Langmuir equation was Rl, and from this study, the values of all Rl were between 0 and 1, indicating that the adsorption process of heavy metals by both activated CNPs and non-activated CNPs was favorable. The Langmuir equation also has Kl, indicating the free energy of adsorption and the affinity of the binding sites. From all the heavy metals tested, the non-activated CNPs had the highest Kl (5,000 L/mg) for Cu adsorption, meaning that there were large amounts of free adsorption energy and

Table 4 | Measured parameters in Freundlich and Langmuir adsorption isotherms

		Adsorption isotherms	
Heavy metals	**Nanomaterial types**	**Langmuir**	**Freundlich**
Cu	Activated CNPs	$y = 0.0013x - 0.0002$ $q_m = 769.23077(mg/g)$ $K_l = 6.5$ (L/mg) Rl = 0.0121 $R^2 = 1$	$y = -0.1202x + 2.962$ $K_f = 916.2205$ ((mg/g) $(L/mg^{-1}))^{1/n}$ $1/n_f = 8.31947$ $N = 0.1202$ $R^2 = 1$
	Non-activated CNPs	$y = 0.001x - 0.0000002$ $q_m = 1{,}000$ (mg/g) $K_l = 5{,}000$ (L/mg) Rl = 0.00001592 $R^2 = 1$	$y = -0.0044x + 2.9926$ $K_f = 983.1052$ ((mg/g) $(L/mg^{-1}))^{1/n}$ $1/n_f = 227.2727$ $N = 0.0044$ $R^2 = 1$
	Activated CNPs/Non-activated CNPs	$y = 0.0012x - 0.00003$ $q_m = 833.333$ (mg/g) $K_l = 40$ (L/mg) Rl = 0.001986 $R^2 = 0.9983$	$y = -0.0387x - 2.9509$ $K_f = 869.561$ ((mg/g) $(L/mg^{-1}))^{1/n}$ $1/n_f = 25.8398$ $N = 0.0387$ $R^2 = 0.884$
Pb	Activated CNPs	$y = 0.0011x - 0.000009$ $q_m = 1{,}000$ (mg/g) $K_l = 1{,}000$ (L/mg) Rl = 0.00008944 $R^2 = 1$	$y = 0.001x - 0.000001$ $K_f = 964.9393$ ((mg/g) $(L/mg^{-1}))^{1/n}$ $1/n_f = 96.1538$ $N = 0.0104$ $R^2 = 1$
	Non-activated CNPs	$y = -0.0104x + 2.9845$ $q_m = 909.0909$ (mg/g) $K_l = 122.22$ (L/mg) Rl = 0.000731 $R^2 = 1$	$y = -0.029x + 2.9721$ $K_f = 937.778$ ((mg/g) $(L/mg^{-1}))^{1/n}$ $1/n_f = 34.4828$ $N = 0.029$ $R^2 = 1$
	Activated CNPs/Non-activated CNPs	$y = 0.001x - 0.000006$ $q_m = 1{,}000$ (mg/g) $K_l = 250$ (L/mg) Rl = 0.000358 $R^2 = 0.9998$	$y = -0.0153x + 2.9794$ $K_f = 953.6741$ ((mg/g) $(L/mg^{-1}))^{1/n}$ $1/n_f = 65.3595$ $N = 0.0153$ $R^2 = 0.8781$
Fe	Activated CNPs	$y = 0.0011x - 0.000005$ $q_m = 909.091$ (mg/g) $K_l = 220$ (L/mg) Rl = 0.00052 $R^2 = 1$	$y = -0.0252x + 2.9704$ $K_f = 934.114$ ((mg/g) $(L/mg^{-1}))^{1/n}$ $1/n_f = 39.6825$ $N = 0.0252$ $R^2 = 1$
	Non-activated CNPs	$y = 0.0013x - 0.0002$ $q_m = 769.2308$ (mg/g) $K_l = 6.5$ (L/mg) Rl = 0.01726 $R^2 = 1$	$y = -0.1405 + 2.9474$ $K_f = 885.9312$ ((mg/g) $(L/mg^{-1}))^{1/n}$ $1/n_f = 7.1174$ $N = 0.1405$ $R^2 = 1$
	Activated CNPs/Non-activated CNPs	$y = 0.0012x - 0.00003$ $q_m = 833.333$ (mg/g) $K_l = 40$ (L/mg) Rl = 0.002846 $R^2 = 0.9995$	$y = -0.0544x + 2.9473$ $K_f = 885.7272$ ((mg/g) $(L/mg^{-1}))^{1/n}$ $1/n_f = 18.3824$ $N = 0.0544$ $R^2 = 0.9267$
Zn	Activated CNPs	$y = 0.0024x - 0{,}0013$ $q_m = 416.667$ (mg/g) $K_l = 1.846$ (L/mg) Rl = 0.11472 $R^2 = 1$	$y = -0.551x + 2.904$ $K_f = 801.678$ ((mg/g) $(L/mg^{-1}))^{1/n}$ $1/n_f = 1.81488$ $N = 0.551$ $R^2 = 1$

(*continued*)

Table 4 | continued

Heavy metals	Nanomaterial types	Adsorption isotherms	
		Langmuir	**Freundlich**
	Non-activated CNPs	$y = 0.0022x - 0.001$ $q_m = 454.5454$ (mg/g) $K_l = 2.2$ (L/mg) Rl = 0.098078 $R^2 = 1$	$y = -0.4973x + 2.894$ $K_f = 783.971$ ((mg/g) $(L/mg^{-1}))^{1/n}$ $1/n_f = 2.010859$ $N = 0.4973$ $R^2 = 1$
	Activated CNPs/Non-activated CNPs	$y = 0.0022x - 0.001$ $q_m = 454.545$ (mg/g) $K_l = 2.2$ (L/mg) Rl = 0.09808 $R^2 = 0.9999$	$y = -0.4944x + 2.8941$ $K_f = 783.6101$ ((mg/g) $(L/mg^{-1}))^{1/n}$ $1/n_f = 2.02265$ $N = 0.4944$ $R^2 = 0.9997$

binding-site affinity of Cu with the surface of the non-activated CNPs. According to Aljeboree *et al.* (2017), the value of Kl decreased with the increase in temperature.

Other measured parameters under the Freundlich equation were Kf (the Freundlich affinity constant) and N (the exponential constant). The values of Kf for all the adsorbents were considered high, with the lowest value being 783.91 ((mg/g) $(L/mg^{-1}))^{1/n}$ (Zn adsorbate and non-activated CNPs adsorbent). According to Solic *et al.* (2020), the significant difference between Kl and Kf demonstrated the presence of selective adsorbents of heavy metals due to the different affinities of the binding sites. Both the activated CNPs and the non-activated CNPs had N values < 1, indicating favorable adsorption. It is also assumed that the process of adsorption for heavy metals was undertaken by the chemical process due to $N < 1$. Martins *et al.* (2015) reported that the N parameter, aka the heterogeneity factor, was also used for evaluation when the adsorption process was physical ($N > 1$), chemical ($N < 1$), or linear ($N = 1$). From this study, the process of adsorption, which was considered through a chemical process, may have been affected by the electrostatic attractions, the van der Waals, and the hydrophobic interactions of both the activated CNPs and the non-activated CNPs. This was in line with the possible cause of the aggregation of the CNPs. Furthermore, the presence of aggregations could lead to an increase in pore size and active sites through the formation of grooves, interstitials, interiors, and exterior sites.

CONCLUSIONS

Through the activation process, the external surfaces of the activated CNPs were irregular without aggregation and were almost circular. As analyzed according to their particle size distribution, the non-activated CNPs had a higher Z-average and size distribution by number, volume, and intensity than those of the activated CNPs, due to the aggregation of their nanofibers. Some of the chemical functional groups of the CNPs were changed. The crystallinity index and the domain of activated CNPs were also higher than those of the non-activated CNPs. Both the activated and the non-activated CNPs had the potential to remove heavy metals, including Cu, Pb, Zn, and Fe.

ACKNOWLEDGEMENTS

All the authors would like to thank SEAMEO BIOTROP for providing financial support with a scheme of SEAMEO BIOTROP Research Grant 2019 and a contract number of 039.6/PSRP/SC/SPK-PNLT/II/2019. We are so grateful to Dr Irdika Mansur, MSc. For.Trop, and Mr Aslan, Ph.D. for giving valuable and imperative inputs to this research. The authors also would like to thank the Indonesia Toray Science Foundation for the supplementary financial support granted to us with a scheme of the 2019 ITSF's Science & Technology Research Grant. Furthermore, we thank Indonesian governmental institutions due to the tremendous and boundless support for this research completion, such as IPB University, Gadjah Mada University, Indonesian Institute of Sciences, Bandung Institute of Technology, Ministry of Environment and Forestry Republic of Indonesia, and Indonesian National Nuclear Agency.

CONFLICT OF INTEREST

There are no conflicts of interest to be declared by the authors.

AUTHOR CONTRIBUTIONS

Ms Salma Zubaidah, Mr Januard Kristian Sihombing, Mr Muhammad Naufal Ibrahim Prabowo, Ms Isna Maulida, and Mr Imam Hermawan conducted laboratory studies on CNP isolation, whereas Ms Nela Rahmati Sari assisted the activation process of CNPs. Mr Saptadi Darmawan, Ms Elis Nina Herliana, and Ms Adisti Permatasari Putri Hartoyo supervised the research team for the execution of this study. Mr Achmad Solikhin was responsible for drafting and analyzing this manuscript, and he also created the research framework.

DATA AVAILABILITY STATEMENT

All relevant data are included in the paper or its Supplementary Information.

REFERENCES

Ahmad, A., Jini, D., Aravind, M., Parvathiraja, C., Ali, R., Kiyani, M. Z. & Alothman, A. 2020 A novel study on synthesis of egg shell based activated carbon for degradation of methylene blue via photocatalysis. *Arabian Journal of Chemistry* **13** (12), 8717–8722.

Alam, M. D., Muyibi, S. A. & Kamaldin, N. 2008 Production of activated carbon from oil palm empty fruit bunches for removal of zinc. In: *Twelfth International Water Technology Conference, IWTC12 2008 Alexandria, Egypt*.

Al-Dulaimi, A. & Wanrosli, W. D. 2017 Isolation and characterization of nanocrystalline cellulose from totally chlorine free oil palm empty fruit bunch pulp. *Journal of Polymers and the Environment* **25** (2), 192–202.

Aljeboree, A. M., Alshirifi, A. N. & Alkaim, A. F. 2017 Kinetics and equilibrium study for the adsorption of textile dyes on coconut shell activated carbon. *Arabian Journal of Chemistry* **10** (2), S3381–S3393.

Aqel, A., El Nour, K. M. M. A., Ammar, R. A. A. & Al-Warthan, A. 2012 Carbon nanotubes, science and technology part (I) structure, synthesis and characterisation. *Arabian Journal of Chemistry* **5** (1), 1–23.

Arie, A. A., Hadisaputra, L., Susanti, R. F., Devianto, H., Halim, M., Enggar, R. & Lee, J. K. 2017 Synthesis of carbon nano materials originated from waste cooking oil using a nebulized spray pyrolysis. *Journal of Physics: Conference Series* **877** (012020), 1–6.

Arora, B. & Attri, P. 2020 Carbon nanotubes (CNTs): a potential nanomaterial for water purification. *Journal of Composites Sciences* **4** (135), 1–20.

Atif, R. & Inam, F. 2016 Reasons and remedies for the agglomeration of multilayered graphene and carbon nanotubes in polymers. *Beilstein Journal of Nanotechnology* **7**, 1174–1196.

Azmina, M. S., Suriani, A. B., Falina, A. N., Salina, M., Rosly, J. & Rusop, M. 2011 Preparation of palm oil based carbon nanotubes at various ferrocene concentration. *Advanced Materials Research* **364**, 408–411.

Azwar, E., Wan Mahari, W. A., Chuah, J. H., Vo, D. V. N., Ma, N. L., Lam, W. H. & Lam, S. S. 2018 Transformation of biomass into carbon nanofiber for supercapacitor application – a review. *International Journal of Hydrogen Energy* **43**, 20811–20821. doi:10.1016/j.ijhydene.2018.09.111.

Baby, R., Saifullah, B. & Hussein, M. Z. 2019 Palm kernel shell as an effective adsorbent for the treatment of heavy metal contaminated water. *Scientific Report* **9** (18955), 1–11.

Bankole, M. T., Abdulkareem, A. S., Mohammed, I. A., Ochigbo, S. S., Tijanim, J. O., Abubakre, O. K. & Ross, W. D. 2019 Selected heavy metals removal from electroplating wastewater by purified and polyhydroxylbutyrate functionalized carbon nanotubes adsorbents. *Scientific Reports* **9** (4475), 1–9.

Bian, Y., Bian, Z.-Y., Zhang, J.-X., Ding, A.-Z., Liu, S.-L. & Wang, H. 2015 Effect of the oxygen-containing functional group of graphene oxide on the aqueous cadmium ions removal. *Applied Surface Science* **329**, 269–275.

Chen, X. W., Timpe, O., Hamid, S. B. A., Schlögl, R. & Su, D. S. 2009 Direct synthesis of carbon nanofibers on modified biomass-derived activated carbon. *Carbon* **47** (1), 340–343.

Darmawan, S. 2014 *Nanoporous Carbon Derived From Forest Biomass Through the Staged Carbonization: Pyrolysis, Hydrothermal and Activation. Dissertation*, Graduate Student of IPB University, Bogor, Indonesia.

Deraman, M., Saad, S. K. M., Ishak, M. M., Awitdrus, A., Taer, E., Talib, I., Omar, R. & Jumali, M. H. H. 2010 Carbon/carbon nanotubes (CNTs) composites from green pellets contain CNTs and self-adhesive carbon grains from fibres of oil palm empty fruit bunch. In *AIP Conference Proceedings* 1284: 175-179.

Elias, M. A., Hadibarata, T. & Sathishkumar, P. 2021 Modified oil palm industry solid waste as a potential adsorbent for lead removal. *Environmental Chemistry and Ecotoxicology* **3**, 1–7.

Faccini, M., Borja, G., Boerrigter, M., Martín, D. M., Crespiera, S. M., Campos, S. V., Aubouy, L. & Amantia, D. 2015 Electrospun carbon nanofiber membranes for filtration of nanoparticles from water. *Journal of Nanomaterials* **2015**, 1–9.

Fan, Q.-Q., Qin, Z.-Y., Liang, X., Li, L., Wu, W.-H. & Zhu, M. F. 2010 Reducing defects on multi-walled carbon nanotube surfaces induced by low-power ultrasonic-assisted hydrochloric acid treatment. *Journal of Experimental Nanoscience* **5** (4), 337–347.

Farma, R., Deraman, M., Awitdrus, A., Talib, I. A., Taer, E., Basri, N. H., Manjunatha, J. G., Ishak, M. M., Dollah, B. N. M. & Hashmi, S. A. 2013 Preparation of highly porous binderless activated carbon electrodes from fibres of oil palm empty fruit bunches for application in supercapacitors. *Bioresource Technology* **132**, 254–261.

Farma, R., Fatjrin, D., Awitdrus & Deraman, M. 2017 Physical properties of activated carbon from fibers of oil palm empty fruit bunches by microwave assisted potassium hydroxide activation. *AIP Conference Proceedings* **1801**, 040001–040004.

Goh, K. Y., Ching, Y. C., Chuah, C. H., Abdullah, L. C. & Liou, N.-S. 2016 Individualization of microfibrillated celluloses from oil palm empty fruit bunch: comparative studies between acid hydrolysis and ammonium persulfate oxidation. *Cellulose* **23**, 379–390.

Ichriani, G. I., Nion, Y. A., Chotimah, H. E. N. C. & Jem, R. 2016 Utilization of oil palm empty bunches waste as biochar-microbes for improving availability of soil nutrients. *Journal of Degraded and Mining Lands Management* **3** (2), 517–520.

Jahangiri, M., Adl, J., Shahtaheri, S. J., Rashidi, A., Ghorbanali, A., Kakooe, H., Forushan, A. R. & Ganjali, M. R. 2013 Preparation of a new adsorbent from activated carbon and carbon nanofiber (AC/CNF) for manufacturing organic-vacbpour respirator cartridge. *Iranian Journal of Environmental Health Science & Engineering* **10** (1), 1–8.

Jovanovic, S., Markovic, Z., Kleut, D., Romcevic, N., Cincovic, M. M., Dramicanin, M. & Markovic, B. T. 2009 Functionalization of single wall carbon nanotubes by hydroxyethyl cellulose. *Acta Chim. Slov.* **56**, 892–899.

Keinänen, P., Siljander, S., Koivula, M., Sethi, J., Sarlin, E., Vuorinen, J. & Kanerva, M. 2018 Optimized dispersion quality of aqueous carbon nanotube colloids as a function of sonochemical yield and surfactant/CNT ratio. *Heliyon* **4** (9), e00787.

Koh, B. & Cheng, W. 2014 Mechanisms of carbon nanotube aggregation and the reversion of carbon nanotube aggregates in aqueous medium. *Langmuir* **30** (36), 10899–10909.

Li, H. & Qiu, Y. 2019 Dispersion, sedimentation and aggregation of multi-walled carbon nanotubes as affected by single and binary mixed surfactants. *Royal Society Open Science* **6** (7), 190241.

Li, S., Gong, Y., Yang, Y., He, C., Hu, L., Zhu, L., Shu, L. & Shu, D. 2015 Recyclable CNTs/Fe_3O_4 magnetic nanocomposites as adsorbents to remove bisphenol A from water and their regeneration. *Chemical Engineering Journal* **260**, 231–239.

Liang, H.-W., Cao, X., Zhang, W.-J., Lin, H.-T., Zhou, F., Chen, L.-F. & Yu, S.-H. 2011 Robust and highly efficient free-standing carbonaceous nanofiber membranes for water purification. *Advanced Functional Materials* **21** (20), 3851–3858.

Liu, D., Wang, Y., Jia, B., Wei, J., Liu, C., Zhu, J., Tang, S., Wu, Z. & Chen, G. 2020 Microwave-assisted hydrothermal preparation of corn straw hydrochar as supercapacitor electrode materials. *ACS Omega* **5**, 26084–26093.

Maddah, B., Soltaninezhad, M., Adib, K. & Hasanzadeh, M. 2016 Activated carbon nanofiber produced from electrospun PAN nanofiber as a solid phase extraction sorbent for the preconcentration of organophosphorus pesticides. *Separation Science and Technology* **52** (4), 700–711.

Mamun, A. A., Ahmed, Y. M., Muyibi, S. A., Al-Khatib, M. F. R., Jameel, A. T. & Al Saadi, M. A. 2016 Synthesis of carbon nanofibers on impregnated powdered activated carbon as cheap substrate. *Arabian Journal of Chemistry* **9** (4), 532–536.

Mamun, A. A., Ahmed, Y. M., Khatib, F. R. A., Jameel, A. T. & Saadi, M. A. A. 2018 The optimum condition for the synthesis of carbon nanofibers on activated carbon to remove lead from aqueous solution. *International Journal of Nanoelectronics and Materials* **1292**, 135–144.

Martins, A. C., Pezoti, O., Cazetta, A. L., Bedin, K. C., Yamazaki, D. A. S., Bandoch, G. F. G., Asefa, T., Visentainer, J. V. & Almeida, V. C. 2015 Removal of tetracycline by NaOH-activated carbon produced from macadamia nut shells: kinetic and equilibrium studies. *Chemical Engineering Journal* **260**, 291–299.

Misra, A., Tyagi, P., Rai, P. & Misra, D. S. 2007 FTIR spectroscopy of multiwalled carbon nanotubes: a simple approach to study the nitrogen doping. *Journal of Nanoscience and Nanotechnology* **7** (6), 1820–1823.

Mubarak, N. M., Sahu, J. N., Abdullah, E. C. & Jayakumar, N. S. 2013 Removal of heavy metals from wastewater using carbon nanotubes. *Separation & Purification Reviews* **43** (4), 311–338.

Niyogi, S., Boukhalfa, S., Chikkannanavar, S. B., McDonald, T. J., Heben, M. J. & Doorn, S. K. 2007 Selective aggregation of single-walled carbon nanotubes via salt addition. *Journal of the American Chemical Society* **129** (7), 1898–1899.

Osman, N. B., Shamsuddin, N. & Uemura, Y. 2016 Activated carbon of oil palm empty fruit bunch (EFB): Core and Shaggy. *Procedia Engineering* **148**, 758–764.

Osman, A. I., Blewitt, J., Abu-Dahrieh, J. K., Farrell, C., Al-Muhtaseb, A. H., Harrison, J. & Rooney, D. W. 2019 Production and characterisation of activated carbon and carbon nanotubes from potato peel waste and their application in heavy metal removal. *Environmental Science and Pollution Research* **26**, 37228–37241.

Pari, G., Darmawan, S. & Prihandoko, B. 2014 Porous carbon spheres from hydrothermal carbonization and KOH activation on cassava and tapioca flour raw material. *Procedia Environmental Sciences* **20**, 342–351.

Park, C., Engel, E. S., Crowe, A., Gilbert, T. R. & Rodriguez, N. M. 2000 Use of carbon nanofibers in the removal of organic solvents from water. *Langmuir* **16** (21), 8050–8056.

Perez-Salcedo, K. Y., Ruan, S., Su, J., Shi, X., Kannan, A. M. & Escobar, B. 2020 Seaweed-derived KOH activated biocarbon for electrocatalytic oxygen reduction and supercapacitor applications. *Journal of Porous Materials* **27**, 959–969. doi:10.1007/s10934-020-00871-7.

Romanos, J., Beckner, M., Rash, T., Firlej, L., Kuchta, B., Yu, P., Suppes, G., Wexler, C., Suppes, G., Wexler, C. & Pfeifer, P. 2011 Nanospace engineering of KOH activated carbon. *Nanotechnology* **23** (015401), 1–7.

Santhosh, C., Nivetha, R., Kollu, P., Srivastava, V., Sillanpää, M., Grace, A. N. & Bhatnagar, A. 2017 Removal of cationic and anionic heavy metals from water by 1D and 2D-carbon structures decorated with magnetic nanoparticles. *Scientific Reports* **7** (1), 1–11.

Smolka, W., Panek, A., Gubernat, M., Fraczek, A. S., Jelen, P., Paluszkiewicz, C., Markowski, J. & Blazewicz, M. 2019 Structure and biological properties of surface-engineered carbon nanofibers. *Journal of Nanomaterials* **2019**, 1–14.

Solic, M., Meletic, S., Isakovski, M. K., Nikic, J., Waston, M., Konya, Z. & Trickovic, J. 2020 Comparing the adsorption

performance of multiwalled carbon nanotubes oxidized by varying degrees for removal of low levels of copper, nickel and chromium (VI) from aqueous solutions. *Water* **12** (723), 1–18.

Tummala, N. R. & Striolo, A. 2009 SDS surfactants on carbon nanotubes: aggregate morphology. *ACS Nano* **3** (3), 595–602.

Wahi, R., Ngaini, Z. & Jok, V. U. 2009 Removal of mercury, lead, and copper from aqueous solution by activated carbon of palm oil empty fruit bunch. *World Applied Sciences Journal* **5**, 84–94.

Yang, X., Wan, Y., Zheng, Y., He, F., Yu, Z., Huang, J., Wang, H., Ok, Y. S., Jiang, Y. & Gao, B. 2019 Surface functional groups of carbon-based adsorbents and their roles in the removal of heavy metals from aqueous solutions: a critical review. *Chemical Engineering Journal* **366**, 608–621.

Ye, R., Cai, J., Pan, Y., Qiao, X. & Sun, W. 2020 Microporous carbon from malva nut for supercapacitors: effects of primary carbonizations on structures and performances. *Diamond and Related Materials* **105** (107816), 1–8.

Yusoff, M. E. M., Idris, J., Zainal, N. H., Ibrahim, M. F. & Abd-Aziz, S. 2019 Adsorption of heavy metal ions by oil palm decanter cake activated carbon. *Makara Journal of Technology* **23** (2), 1–8.

First received 19 January 2021; accepted in revised form 15 April 2021. Available online 29 April 2021